(a)

(b)

Fig. 6 Comparison of the regurgitant flows obtained at four different types of ePTFE valves and a Björk–Shiley Monostrut (BSM) used as a control under pump rates of **a** 60 bpm and **b** 120 bpm

Table 1 Comparison of the mean flow rate obtained when using four different types of ePTFE valves at a pump rate of 60 bpm

Valve	Mean flow rate (ml/min)
BSM (control)	7.0×10^2
B(+)F(+)	7.4×10^2
B(+)F(−)	7.0×10^2
B(−)F(+)	7.0×10^2
B(−)F(−)	6.8×10^2

B(+) valve with bulging sinuses, B(−) straight valve without bulging sinuses, F(+) fan-shaped leaflet, F(−) unfan-shaped leaflet

Table 2 Comparison of the mean flow rate obtained when using four different types of ePTFE valves at a pump rate of 120 bpm

Valve	Mean flow rate (ml/min)
BSM (control)	9.5×10^2
B(+)F(+)	1.0×10^3
B(+)F(−)	1.0×10^3
B(−)F(+)	9.5×10^2
B(−)F(−)	8.7×10^2

B(+) valve with bulging sinuses, B(−) straight valve without bulging sinuses, F(+) fan-shaped leaflet, F(−) unfan-shaped leaflet

Reynolds number in order to investigate velocity profiles from the data on the effective orifice area (Eq. 3):

$$A_{EO} = \frac{q_{v_{RMS}}}{51.6 \times \sqrt{\frac{\Delta p}{\rho}}}, \qquad (2)$$

where A_{EO} is the effective orifice area, $q_{v_{RMS}}$ is the root mean square flow, and ρ is the density of the fluid.

$$R_e = \frac{\overline{V}D}{v} = 16.56 \frac{(\text{volumeflow})}{A_{EO}}, \qquad (3)$$

where R_e is the Reynolds number, $\overline{V}$ is the mean flow rate, and D is the tube diameter.

Results

Regurgitation and pressure gradients of the valves

In the first approach, valvular regurgitant flow was obtained in the pulmonary circulatory system that we developed. The control data exhibited typical pediatric pulmonary hemodynamics when the monoleaflet mechanical heart valve was installed at the outflow portion of the ventricular model. As shown in Fig. 6, the regurgitant flows in the B(+) groups were smaller than those in the B(−) groups, regardless of the shape of the leaflet. In the B(+) groups, regurgitation with the fan-shaped leaflets and that with the unfan-shaped leaflets were 45 and 29 ml/min, respectively, at a pump rate of 120 bpm, whereas the value obtained with the monoleaflet valve was 100 ml/min. The regurgitant flow was approximately 40% lower than that of the control at any pump rate. The mean flow measured with B(+) was 1.0×10^3 ml/min, which was 5% bigger than that of the control at a pump rate of 120 bpm, as shown in Tables 1 and 2.

Transvalvular pressure gradients and energy losses at the valves

With the fan-shaped B(+) valve, the transvalvular pressure gradients measured at pump rates of 60 and 120 bpm were 1.1 ± 0.1 and 1.2 ± 0.1 mmHg, respectively, whereas those obtained with the fan-shaped B(−) valves were 6.8 ± 0.1 and 6.4 ± 0.1 mmHg. However, the transvalvular pressure gradients were elevated for the valves with unfan-shaped leaflets, and was always bigger than ~ 4 mmHg, as shown in Fig. 7.
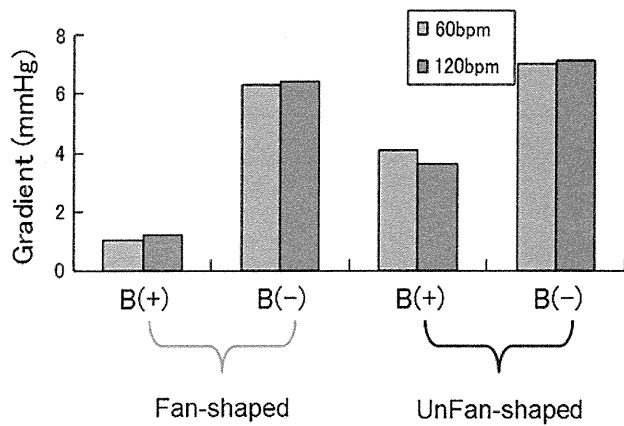
Fig. 7 For the valves with unfan-shaped leaflets, the transvalvular pressure gradient was elevated and was always bigger than ~ 4 mmHg
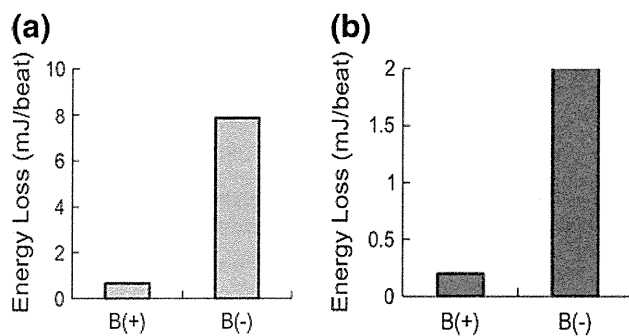

Fig. 8 Losses of transvalvular energy with the valve with bulging sinuses (i.e., B(+)) and fan-shaped leaflets, and with the valve in a straight conduit (i.e., B(−)) with fan-shaped leaflets, under pump rates of **a** 60 bpm and **b** 120 bpm
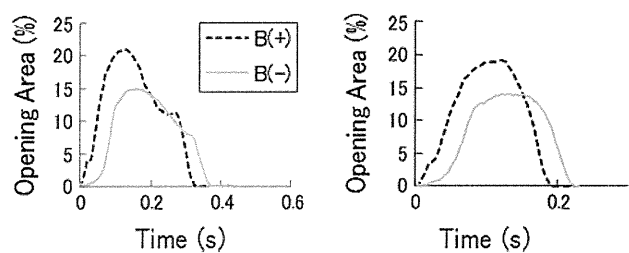

Fig. 9 Changes in the valve opening area obtained for the valve with bulging sinuses (i.e., B(+)) and fan-shaped leaflets, and the straight valve without bulging sinuses (i.e., B(−)) and fan-shaped leaflets

For the valves with fan-shaped leaflets, the relative loss of transvalvular energy loss with the B(+) valve was found to be significantly lower than that for the B(−) valve, as shown in Fig. 8.

Valve leaflet movement

Figure 9 shows the changes in the opening areas of the valves with fan-shaped leaflets, as calculated from the pictures obtained sequentially with the video camera.

Table 3 Reynolds numbers calculated from data on the valve opening area and the maximum systolic flow velocity

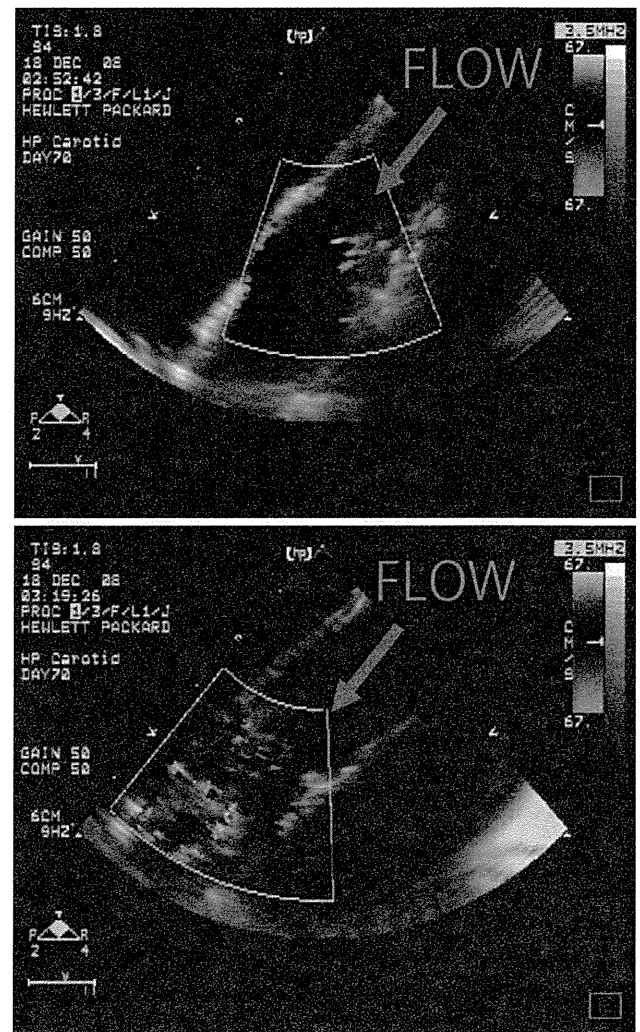| Valve/pump rate (bpm)	Reynolds number
B(+)F(+)/60	1639
B(+)F(+)/120	1668
B(−)F(+)/60	2378
B(−)F(+)/120	2454

Fig. 10 Doppler echocardiographic investigations of the vicinity of the valve leaflet for the valve with bulging sinuses (B(+)) (**a**) the straight valve without bulging sinuses (B(−)) (**b**)

The data were normalized to the valve conduit diameter. Each waveform was triggered and synchronized to the contraction signal for the right ventricular pneumatic driver. The movements in the B(+) valve were found to occur earlier than those in the B(−) valve. Moreover, the valve opening area in the B(+) valve was $\sim 35\%$ greater than that for the B(−) valve.

Changes in the Reynolds number

When the Reynolds numbers were calculated from the data on effective orifice area and root mean square flow rate through the valves, we found that the valves with bulging sinuses gave smaller Reynolds numbers than those without bulging sinuses, at all pump rates, as shown in Table 3 and Fig. 9. The Reynolds numbers for the valves with bulging sinuses were less than 1700. Moreover, a uniform rotational fluid velocity was not present in the valves without bulging sinuses, based on the results of a Doppler echocardiographic examination.

Flow characteristics in the vicinity of the leaflets

We used Doppler flow velocimetry to analyze the Doppler flow distribution in the vicinity of the leaflets in valves with and without bulging sinuses. The Doppler flow distributions are presented in Fig. 10. As the direction of the flow velocity in the M-mode indicates the behavior of the ring, as shown in Fig. 10a (i.e., B(+)), the results indicated that a large eddy formed in the vicinity of the leaflets when the valve with bulging sinuses was studied. On the other hand, in the B(−) valve, there was a small jet in the distal portion of the valve, and turbulent flow was produced, as shown in Fig. 10b [5, 6].

Discussion

In this study, we measured the hemodynamic characteristics of the ePTFE valve in our pulmonary mechanical circulatory system. Our results support the current idea that the bulging sinuses of the ePTFE valve promote dynamic leaflet movement. In our mechanical circulatory system that simulates natural pediatric pulmonary hemodynamics, Doppler echocardiography investigations indicated that the fluid downstream curled back toward the ventricle to form a large eddy that spins in the vicinity of the leaflets with the bulging sinuses. The Reynolds number calculated from the valve opening area and the systolic transvalvular flow velocity is consistent with the phenomena observed using echocardiographic velocimetry. The data in Table 3 clearly indicate that the smaller opening area at the valve in the straight tubing induces a higher transvalvular velocity in systole, and the jet through the valve then interferes with the formation of the large eddy or vortex downstream of the leaflets.

The transvalvular energy losses through the valves with fan-shaped leaflets showed that the bulging sinuses eliminated valvular resistance in systole. Although we observed slight increases in the mean flow in the valves with bulging sinuses, significant decreases in the energy losses through the valves were associated with the transvalvular pressure gradient. This suggests that the pulmonary ePTFE valve with bulging sinuses provides effective unloading of the right ventricular pumping function. Regarding the dynamic analysis of the valve orifice area according to leaflet movement, the B(−) valves showed the larger fluctuations during systole than the B(+) valves, due to leaflet fluttering.

The applicability of the valve design should be also considered in relation to regurgitation, especially in smaller patients. The regurgitant flow in a valve is related to the valvular dynamic response and leaflet movements, and we found that the use of unfan-shaped leaflets decreased the regurgitant flow in any conduit structure in this study. These results suggest that the leaflet design is one of the important parameter to achieve more sophisticated valvular function.

Our study investigated changes in leaflet motion, which were determined by a high-speed camera focused on the visualization chamber. As measurements of valvular movement were carried out by the mechanical circulatory system using water at room temperature, we cannot apply all these fluid dynamic characteristic results in the valves employed here to clinical cases of congenital heart disease with hemorheological variations. Future studies are planned to evaluate the fluttering effects of the leaflets or cusps under higher fluid viscosity conditions. A future study will examine the consequences of varying the hemodynamic conditions in order to determine the effect of the fluid viscosity on the mechanical motion of the leaflets, as well as the characteristics of the fluid, such as a vortex or eddy in the vicinity of the valve.

Since the ePTFE valves employed in this study were handmade, it was anticipated that there could be variations in the shapes or the sutures in the valves. We evaluated the effects of bulging sinuses in the conduit on the hemodynamic function, and concluded that bulging sinuses in the conduit can eliminate energy losses, regardless of the leaflet design (fan-shaped and unfan-shaped).

In summary, our experimental study in the mock circulatory system confirmed the effectiveness of using bulging sinuses in ePTFE pulmonary valves.

Conclusion

In this study, we performed hemodynamic examinations of ePTFE pulmonary heart valves in a pediatric mechanical circulatory system. In terms of optimizing the valvular hemodynamic function, we found that any such sophisticated valved conduit should employ bulging sinuses for eliminating regurgitation and transvalvular energy loss.

References

1. Fiore AC, Peigh PS, Robison RJ, Glant MD, King H, Brown JW. Valved and nonvalved right ventricular–pulmonary arterial extracardiac conduits. An experimental comparison. J Thorac Cardiovasc Surg. 1983;86:490–7.
2. Ando M, Imai Y, Hoshino S, Ishihara K. Autologous reconstruction of pulmonary trunk at reoperation after extracardiac conduit repair. Ann Thorac Surg. 1995;59:621–5.
3. Ando M, Takahashi Y. Ten-year experience with handmade trileaflet polytetrafluoroethylene valved conduit used for pulmonary reconstruction. J Thorac Cardiovasc Surg 2009;137:124–131.
4. Brown JW, Ruzmetov MR, Rodefeld MD, Vijay P, Turrentine MW. Right ventricular outflow tract reconstruction with an allograft conduit in non-Ross patients: risk factors for allograft dysfunction and failure. Ann Thorac Surg. 2005;80:655–64.
5. Dur O, Yoshida M, Manor P, Mayfield A, Wearden PD, Morell VO, Pekkan K. In vitro evaluation of right ventricular outflow tract reconstruction with bicuspid valved polytetrafluoroethylene conduit. Artif Organs. 2010;34:1010–6.
6. Molina JE. Preliminary experience with GORE-TEX grafting for right ventricle–pulmonary artery conduits. Tex Heart Inst J. 1986;13:137–42.
7. Elkins RC. The Ross operation: a 12-year experience. Ann Thorac Surg. 1999;68:S14–8.
8. Bielefeld MR, Bishop DA, Campbell DN, Mitchell MB, Grover FL, Clarke DR. Reoperative homograft right ventricular outflow tract reconstruction. Ann Thorac Surg. 2001;71:482–8.
9. Oosterhof T, Meijboom FJ, Vliegen HW, Hazekamp MG, Zwinderman AH, Bouma BJ, van Dijk AP, Mulder BJ. Long-term follow-up of homograft function after pulmonary valve replacement in patients with tetralogy of Fallot. Eur Heart J. 2006;27:1478–84.
10. Iwai S, Torikai K, Coppin CM, Sawa Y. Minimally immunogenic decellularized porcine valve provides in situ recellularization as a stentless bioprosthetic valve. J Artif Organs. 2007;10:29–35.
11. Sekarski N, van Meir H, Rijlaarsdam MEB, Schoof PH, Koolbergen DR, Hruda J, von Segesser LK, Meijboom EJ, Hazekamp MG. Right ventricular outflow tract reconstruction with the bovine jugular vein graft: 5 years' experience with 113 patients. Ann Thorac Surg. 2007;84:599–605.
12. Boethig D, Goerler H, Wasthoff-Bleck M, Ono M, Daiber A, Haverich A, Breymann T. Evaluation of 188 consecutive homografts implanted in pulmonary position after 20 years. Eur J Cardiothorac Surg. 2007;32:133–42.
13. Tokunaga S, Masuda M, Shiose A, Tomita Y, Morita S, Tominaga R. Isolated pulmonary valve replacement: analysis of 27 years of experience. J Artif Organs. 2008;11:130–3.
14. Brown JW, Ruzmetov MR, Estayeb O, Rodefeld MD, Turrentine MW. Performance of SynerGraft decellularized pulmonary homograft in patients undergoing a Ross procedure. Ann Thorac Surg. 2011;91:416–23.
15. Yamagishi M, Emoto T, Wada Y, Oka T. Pulmonary reconstruction in the Ross procedure. Combined autologous aortic and polytetrafluoroethylene valve. J Thorac Cardiovasc Surg. 1998;116:1076–7.
16. Miyazaki T, Yamagishi M, Maeda Y, Yamamoto Y, Taniguchi S, Sasaki Y, Yaku H. Expanded polytetrafluoroethylene conduits and patches with bulging sinuses and fan-shaped valves in right ventricular outflow tract reconstruction: multicenter study in Japan. J Thorac Cardiovasc Surg. 2011; [Epub ahead of print].
17. Peacock JA. An in vitro study of the onset of turbulence in the sinus of Valsalva. Circ Res. 1990;67:448–80.
18. Yamanami M, Yahata Y, Tajikawa T, Ohba K, Watanabe T, Kanda K, Yaku H, Nakayama Y. Preparation of in vivo tissue-engineered valved conduit with the sinus of Valsalva. J Artif Organs. 2010;13:106–12.
19. Cooke J, Hertzberg J, Boardman M, Shandas R. Characterizing vortex ring behavior during ventricular filling with Doppler echocardiography: an in vitro study. Ann Biomed Eng. 2004;32:245–56.
20. Tanaka M, Sakamoto T, Sugawara S, Nakajima H, Katahira Y, Ohtsuki S, Kanai H. Blood flow structure and dynamics, and ejection mechanism in the left ventricle: analysis using echocardiography. J Cardiol. 2008;52:86–101.
21. Yap CH, Dasi LP, Yoganathan AP. Dynamic hemodynamic energy loss in normal and stenosed aortic valves. J Biomech Eng. 2010;132:021005.
22. Yoganathan AP, He Z, Jones C. Fluid mechanics of heart valves. Ann Rev Biomed Eng. 2004;6:331–62.

Metabolomic profiling of the autosomal dominant polycystic kidney disease rat model

Takafumi Toyohara · Takehiro Suzuki · Yasutoshi Akiyama · Daisuke Yoshihara ·
Yoichi Takeuchi · Eikan Mishima · Koichi Kikuchi · Chitose Suzuki · Masayuki Tanemoto ·
Sadayoshi Ito · Shizuko Nagao · Tomoyoshi Soga · Takaaki Abe

Abstract

Background Autosomal dominant polycystic kidney disease (ADPKD) is an inherited systemic disease characterized by renal cyst expansion, resulting in renal failure. With the progression of renal damage, the accumulation of uremic compounds is recently reported to subsequently cause further renal damage and hypertension. Finding uremic toxins and sensitive markers for detecting the early stage of ADPKD is necessary to clarify its pathophysiological process and to prevent its progression. The aim of this study was to analyze the profile of uremic retention solutes of ADPKD by capillary electrophoresis–mass spectrometry (CE-MS) using the Han:SPRD rat model.

Methods Two hundred and ninety-seven cations and 190 anions were comprehensively analyzed by CE-MS in Han:SPRD rats and control rats.

Results We found 21 cations and 19 anions that accumulated significantly in the heterozygous (Cy/+) ADPKD rat model compared with control rats. Among the compounds, increases in 5-methyl-2'-deoxycytidine, glucosamine, ectoine, allantoate, α-hydroxybenzoate, phenaceturate and 3-phenylpropionate and decreases in 2-deoxycytidine, decanoate and 10-hydroxydecanoate were newly identified in the ADPKD Cy/+ rats.

Conclusion We identified uremic retention solutes in ADPKD Cy/+ rats. Compounds related to ADPKD could be useful markers for detecting the early stage of ADPKD.

Keywords Uremic toxin · ADPKD · CE-MS · Biomarker

T. Toyohara, T. Suzuki and Y. Akiyama contributed equally to this work.

T. Toyohara · T. Suzuki · Y. Akiyama · Y. Takeuchi ·
E. Mishima · K. Kikuchi · C. Suzuki · M. Tanemoto · S. Ito ·
T. Abe
Division of Nephrology, Endocrinology and Vascular Medicine,
Tohoku University, Graduate School of Medicine,
Sendai 980-8574, Japan

D. Yoshihara · S. Nagao
Education and Research Center of Animal Models for Human
Diseases, Fujita Health University, Toyoake 470-1192, Japan

T. Soga
Institute for Advanced Biosciences,
Keio University, Tsuruoka 997-0052, Japan

T. Abe (✉)
Division of Medical Science, Tohoku University Graduate
School of Biomedical Engineering, Sendai 980-8574, Japan
e-mail: takaabe@med.tohoku.ac.jp

Y. Takeuchi · T. Abe
Department of Clinical Biology and Hormonal Regulation,
Tohoku University, Graduate School of Medicine,
Sendai 980-8574, Japan

Introduction

Autosomal dominant polycystic kidney disease (ADPKD) is the most frequent life-threatening hereditary disease, affecting 1 in 500 individuals in Western countries [1, 2]. With the decrease of renal function, the accumulation of uremic toxins has been related to cardiovascular, hematological, neurological and immunological complications [3]. It also leads to difficulty in controlling blood pressure, impaired renal function and worsening prognosis [3–5]. So far, more than 110 organic compounds have been identified as uremic retention solutes [3, 6]; if these compounds are found to have biological harmful activities, they are called uremic toxins.

Recently, Torremans et al. [7] reported the plasma profile of cationic guanidino compounds in ADPKD patients and a rat ADPKD/Mhm model; however, other profiles of cationic and anionic compounds have not been clarified in ADPKD.

Recently, we revealed around 500 anionic and cationic compounds in a rat renal failure model [8] and in human chronic kidney disease (CKD) patients [9] using capillary electrophoresis–mass spectrometry (CE-MS). In CE-MS, metabolites are first separated by capillary electrophoresis (CE) based on charge and size, and then selectively detected using mass spectrometry (MS). This technology enables detection of over 1,000 charged species simultaneously [10]. We also found that the organic anion transporter SLCO4C1 transports asymmetrical dimethylarginine (ADMA), guanidino succinate and *trans*-aconitate, and that the reduction in renal function causes the accumulation of these compounds in renal failure [8, 11].

Accordingly, the aim of this study is to comprehensively analyze the serum from ADPKD Cy/+ rats by CE-MS and identify the pathogenesis of renal damage as well as to find new biomarker(s) for detecting early renal damage in ADPKD.

Materials and methods

Animals

The study was conducted in heterozygous (Cy/+) and normal littermate control (+/+) Han:SPRD rats. All the normal rats and Cy/+ rats studied were male. The Cy/+ Han:SPRD rat develops detectable polycystic kidney disease by 8 weeks of age, as evidenced by a doubling of the kidney size and renal failure compared with +/+ control rats [12, 13]. The University of Fujita Health University Animal Care and Use Committee approved the study protocol.

CE-MS measurement for metabolome analysis

A comprehensive and quantitative analysis of charged metabolites by CE-MS was performed [8, 9, 14]. Plasma (50 μl) was immediately plunged into methanol (450 μl) containing internal standards (20 μM each of methionine sulfone; Wako, Osaka, Japan) for cations, MES (Dojindo, Kumamoto, Japan) and CSA (D-Camphor-10-sulfonic acid, Wako). De-ionized water (200 μl) and chloroform (500 μl) were then added, and the mixture was thoroughly mixed. The solution was centrifuged at 4,600×g for 5 min at 4°C, and the upper aqueous layer was centrifugally filtered through a Millipore 5,000 Da cut-off filter (Millipore, Billerica, MA, USA) to remove proteins. The filtrate was

lyophilized and dissolved in 25 μl of Milli-Q water containing reference compounds (200 μM each of 3-amino-pyrrolidine; Sigma-Aldrich, St. Louis, MO, USA) and trimesate (Wako) prior to CE with electrospray ionization time-of-flight mass spectrometry (CE-TOFMS) analysis. All CE-TOFMS experiments were performed using the Agilent CE capillary electrophoresis system (Agilent Technologies, Waldbronn, Germany), the Agilent G3250AA LC/MSD TOF system (Agilent Technologies, Palo Alto, CA, USA), the Agilent 1100 series binary HPLC pump, the G1603A Agilent CE-MS adapter, and the G1607A Agilent CE-ESI-MS sprayer kit. For data acquisition, we used G2201AA Agilent ChemStation software for CE and the Analyst QS for Agilent TOFMS software [14].

Cationic metabolites were separated in a fused silica capillary (50 μm i.d. × 100 cm) filled with 1 M formic acid as the electrolyte [15]. A sample solution was injected at 50 mbar for 3 s (3 nl) and 30 kV of voltage was applied. The capillary temperature and the sample tray were set at 20°C and below 5°C, respectively. Methanol water (50% v/v) containing 0.1 μM hexakis(2,2-difluoroethoxy)phosphazene was delivered as the sheath liquid at 10 μl/min. ESI-TOFMS was operated in the positive ion mode, and the capillary voltage was set at 4 kV. A flow rate of heated dry nitrogen gas (heater temperature 300°C) was maintained at 10 psig. In TOFMS, the fragmentor, skimmer and Oct RFV voltages were set at 75, 50, and 125 V, respectively. Automatic recalibration of each acquired spectrum was performed using reference masses of reference standards ([^{13}C isotopic ion of protonated methanol dimer (2MeOH+H)]$^+$, m/z 66.0632) and ([hexakis(2,2-difluoroethoxy)phosphazene+H]$^+$, m/z 622.0290). Exact mass data were acquired at a rate of 1.5 spectra/s over a 50–1,000 m/z range.

Anionic metabolites were separated in a COSMO(+), chemically coated with a cationic polymer, capillary (50 μm i.d. × 100 cm) (Nacalai Tesque, Kyoto, Japan) filled with 50 mM ammonium acetate solution (pH 8.5) as the electrolyte [10, 16]. A sample solution was injected at 50 mbar for 30 s (30 nl) and −30 kV of voltage was applied. A platinum electrospray ionization spray needle was replaced with the original Agilent stainless steel needle. 5 mM ammonium acetate in 50% (v/v) methanol–water containing 0.1 μM hexakis(2,2-difluoroethoxy)phosphazene was delivered as the sheath liquid at 10 μl/min. ESI-TOFMS was operated in the negative ion mode, and the capillary voltage was set at 3.5 kV. In TOFMS, the fragmentor, skimmer and Oct RFV voltages were set at 100, 50, and 200 V, respectively. Automatic recalibration of each acquired spectrum was performed using reference masses of reference standards ([^{13}C isotopic ion of deprotonated acetic acid dimer (2CH$_3$COOH−H)]$^-$,

m/z 120.0384 and [hexakis(2,2-difluoroethoxy)phospha-zene+deprotonated acetic acid($CH_3COOH-H$)]$^-$, m/z 680.0355). Other conditions were the same as in cationic metabolite analysis.

Data analysis

Unpaired t test was calculated to assess the difference of the plasma concentrations of the compounds. A value of $P < 0.05$ was accepted as indicating statistical significance.

Results

Biological profiles of Cy/+ rats

Biological profiles of the Cy/+ rats and +/+ rats at 14 weeks old are shown in Table 1. The two groups of rats did not differ in body weight. By contrast, the kidney weight and percentage of kidney weight in body weight (%KB) were 2.96- and 2.95-fold greater in the Cy/+ rats than in the +/+ rats. Serum urea nitrogen (serum UN) was significantly higher in Cy/+ rats compared to +/+ rats, suggesting that Cy/+ rats developed renal failure. The blood pressure of Cy/+ rats was significantly higher than the +/+ rats.

Metabolomic analysis of the Cy/+ ADPKD rat model

Using CE-MS analysis, 312 cationic and 193 anionic compounds whose molecular weights ranged from 73.0 to 460.1 m/z were analyzed and quantified. As a result, 22 cationic and 19 anionic compounds were significantly identified in the ADPKD rats (Tables 2, 3, 4; Figs. 1, 2).

Cations

As shown in Fig. 1a, 19 cationic compounds, γ-guanidino butyric acid (γ-GBA), creatinine, anthranilate, 3-methyl-histidine, allantoin, trimethylamine N-oxide, pipecolate, 5-methyl-2′-deoxycytidine, homoarginine, α-aminoadipate, hydroxyproline, glucosamine, citrulline, ectoine, methionine sulfoxide, Gly, ADMA, N,N-dimethylglycine and

guanidinosuccinic acid (GSA), were significantly increased in Cy/+ rats. On the other hand, as shown in Fig. 1b, three anionic compounds, 2′-deoxycytidine, carnitine and o-acetylcarnitine, were decreased in Cy/+ rats.

The increase of 5-methyl-2′-deoxycytidine, glucosamine and ectoine and the decrease of 2′-deoxycytidine were newly identified [4, 17–27] (Table 4).

Anions

As shown in Fig. 2a, 13 anionic compounds, hippurate, allantoate, citrate, α-hydroxybenzoate, cis-aconitate, iso-citrate, phenaceturate, 3-phenylpropionate, 3-indoxyl sulfate, trans-aconitate, isethionate, pantothenate and pimelate, were increased in the Cy/+ rat model. On the other hand, as shown in Fig. 2b, 6 anionic compounds, decanoate, 2-oxoglutarate, octanoate, 2-oxoisopentanoate, 4-methyl-2-oxopentanoate and 10-hydroxydecanoate, were significantly decreased in the Cy/+ rat model.

The increase of allantoate, α-hydroxybenzoate, phe-naceturate and 3-phenylpropionate and the decrease of decanoate and 10-hydroxydecanoate were newly identified [28–31] (Table 4).

Discussion

This is the first detailed study evaluating the concentrations of anions and cations in ADPKD rats. Although there are few studies revealing the concentration of uremic solutes in ADPKD rats, the concentrations of guanidinosuccinate, creatine, guanidinoacetate, arginine, homoarginine and ADMA in our study are almost in the same range as a previous report [7], suggesting that CE-MS is equally quantitatively established.

By CE-MS, the increased concentrations of cationic compounds 5-methyl-2′-deoxycytidine, glucosamine, ec-toine, and anionic compounds allantoate, α-hydroxyben-zoate, phenaceturate and 3-phenylpropionate were newly identified in ADPKD Cy/+ rats. Simultaneously, the decrease of the cationic compound 2-deoxycytidine and the anionic compound decanoate and 10-hydroxydecanoate was also newly identified in ADPKD Cy/+ rats (italicized compounds in Table 4; group A in Fig. 3). Because the

Table 1 Biological profiles of Cy/+ rats and +/+ rats at 14 weeks old

	Number	Body weight (g)	Kidney weight (g)	%KB	Serum UN (mg/dl)	Blood pressure (mmHg)
Cy/+	5	412 ± 3	8.3 ± 0.3*	2.01 ± 0.08*	83.6 ± 5.0*	180 ± 8*
+/+	5	415 ± 6	2.8 ± 0.0	0.68 ± 0.01	24.3 ± 0.6	148 ± 5

* Significant difference between Cy/+ rats and +/+ rats

Table 2 Seventy cationic compounds detected by CE-MS in +/+ rats and Cy/+ rats

Cationic compound	+/+ rat (μM)	Cy/+ rat (μM)	P value
γ-Guanidinobutyrate	0.62 ± 0.09	3.06 ± 0.17	**<0.001**
Creatinine	23.92 ± 1.42	69.81 ± 4.64	**<0.001**
Anthranilate	2.23 ± 0.35	7.67 ± 0.57	**<0.001**
3-Methylhistidine	13.52 ± 0.99	31.94 ± 2.49	**<0.001**
Allantoin	236.10 ± 5.41	420.98 ± 28.76	**<0.001**
Trimethylamine *N*-oxide	1.49 ± 0.18	4.68 ± 0.54	**0.001**
Pipecolate	3.98 ± 0.47	10.58 ± 1.15	**0.001**
5-Methyl-2'-deoxycytidine	*0.68 ± 0.02*	*0.90 ± 0.04*	*0.002*
Homoarginine; *N*6,*N*6,*N*6-trimethyllysine	1.05 ± 0.07	1.78 ± 0.14	**0.003**
2'-Deoxycytidine	32.31 ± 1.78	23.87 ± 1.41	**0.010**
α-Aminoadipate	1.15 ± 0.13	1.82 ± 0.13	**0.012**
Hydroxyproline	33.49 ± 2.07	57.88 ± 6.43	**0.012**
Glucosamine	*0.65 ± 0.03*	*1.03 ± 0.09*	*0.015*
Citrulline	73.65 ± 5.42	132.47 ± 16.45	**0.016**
Ectoine	*2.00 ± 0.38*	*3.85 ± 0.37*	*0.018*
Methionine sulfoxide	3.84 ± 0.27	5.24 ± 0.33	**0.022**
Gly	193.74 ± 9.44	239.02 ± 10.92	**0.023**
ADMA	0.56 ± 0.05	0.84 ± 0.08	**0.025**
Carnitine	61.11 ± 4.61	44.13 ± 3.38	**0.029**
N,*N*-Dimethylglycine	7.87 ± 0.75	14.39 ± 2.08	**0.030**
o-Acetylcarnitine	3.40 ± 0.28	2.36 ± 0.22	**0.032**
Guanidinosuccinate	ND	0.66 ± 0.13	–
N-Acetylglucosamine	3.86 ± 0.55	5.43 ± 0.33	0.060
Serotonin	6.46 ± 1.04	9.59 ± 0.76	0.061
Creatine	203.71 ± 14.14	139.04 ± 22.59	0.062
Met	53.25 ± 2.51	63.41 ± 3.64	0.074
Taurine	578.55 ± 60.72	734.80 ± 31.47	0.075
Ala	418.32 ± 31.46	519.76 ± 32.02	0.078
Lys	244.25 ± 20.06	295.97 ± 19.38	0.136
His	50.57 ± 1.65	57.76 ± 3.65	0.147
beta-Ala	2.26 ± 0.14	2.83 ± 0.31	0.150
Kynurenine	1.24 ± 0.10	1.55 ± 0.16	0.176
Pro	194.95 ± 12.02	227.67 ± 15.68	0.177
Ornithine	36.38 ± 4.52	54.02 ± 12.02	0.254
Betaine	121.46 ± 4.22	142.97 ± 16.39	0.289
Ser	184.61 ± 4.92	175.36 ± 5.40	0.290
Gln	509.87 ± 20.64	454.20 ± 43.80	0.334
Asp	25.48 ± 3.53	29.94 ± 2.26	0.369
Phe	66.31 ± 4.47	72.22 ± 3.36	0.372
5-Methoxytryptamine; 2,6-diaminoheptanedioate	0.33 ± 0.02	0.40 ± 0.08	0.380
Ethanolamine phosphate	3.50 ± 0.57	2.61 ± 0.09	0.399
Indole-3-acetate	3.88 ± 0.18	4.39 ± 0.48	0.404
Trp	92.38 ± 8.24	81.54 ± 7.80	0.418
Thr	229.95 ± 14.43	249.25 ± 16.43	0.453
5-Oxoproline	25.75 ± 1.26	27.68 ± 1.89	0.469
N-gamma-Ethylglutamine	5.05 ± 0.26	4.76 ± 0.26	0.491
Nicotinamide	3.31 ± 0.15	3.63 ± 0.37	0.499
2-Aminobutyrate	4.38 ± 0.41	3.93 ± 0.42	0.520

🙋 Springer

Table 2 continued

Cationic compound	+/+ rat (μM)	Cy/+ rat (μM)	P value
Cytidine	8.19 ± 0.59	9.05 ± 1.11	0.555
Arg	194.64 ± 8.52	175.80 ± 27.15	0.570
Putrescine (1,4-butanediamine)	0.84 ± 0.12	0.74 ± 0.07	0.634
Sarcosine	5.13 ± 0.63	5.59 ± 0.55	0.635
Glu	141.91 ± 24.13	156.83 ± 13.76	0.644
γ-Butyrobetaine	1.82 ± 0.14	1.69 ± 0.21	0.659
N-epsilon-Acetyllysine	0.91 ± 0.01	0.86 ± 0.06	0.676
Tyr	47.54 ± 2.28	45.99 ± 2.40	0.686
Glutathione(ox) divalent	1.65 ± 0.27	2.16 ± 1.17	0.711
Metformin	0.07 ± 0.02	0.09 ± 0.00	0.712
Cysteine-glutathione disulphide	3.13 ± 0.42	3.50 ± 0.88	0.741
Phosphorylcholine	6.82 ± 1.48	6.07 ± 0.09	0.772
Guanidinoacetate	7.59 ± 0.66	8.07 ± 1.43	0.792
Leu	152.77 ± 14.10	148.03 ± 7.21	0.795
Hypotaurine	9.40 ± 0.94	9.72 ± 0.67	0.812
Val	180.48 ± 14.22	176.90 ± 7.81	0.848
GABA	0.80 ± 0.03	0.82 ± 0.13	0.892
5-Hydroxy-3-indoleaceacetate	1.12 ± 0.09	1.16 ± 0.30	0.937
Asn	66.46 ± 5.81	66.79 ± 5.44	0.972
5-Hydroxylysine	1.08 ± 0.12	1.08 ± 0.12	0.980
Glycerophosphorylcholine	32.14 ± 6.24	32.28 ± 2.26	0.985
Ile	79.67 ± 7.98	79.51 ± 3.30	0.987

These compounds are in an ascending order of P value calculated by t test

A value of $P < 0.05$ is accepted as indicating a significant difference in the compound concentration between +/+ rats and Cy/+ rats (22 cations). Italicized compounds are newly isolated (referred to in Table 4)

concentrations of these compounds were low or not detected in the rat nephrectomy model [8] or human CKD patients [9], these compounds could be a new marker(s) for detecting ADPKD. As shown in a previous study, 5-methyl-2'-deoxycytidine is known as an oxidized nucleotide [32] and allantoate is a urate oxidation product [33]. These compounds may increase as the result of the oxidative state in renal failure. On the other hand, glucosamine was reported as a cytoprotective agent and is able to regulate inflammation [34]. Ectoine works as organic osmolytes and protects cells against high concentration conditions [35]. These compounds may increase to protect cells from inflammatory and high concentration conditions in renal failure; however, further studies are required to elucidate mechanisms by which these compounds increase only in ADPKD rats.

Cationic compounds creatinine, 3-methylhistidine, allantoin, trimethylamine N-oxide, hydroxyproline, citrulline and GSA, and anionic compounds hippurate, 3-indoxyl sulfate, and trans-aconitate were increased in Cy/+ rats, rats in the renal failure model, and CKD patients (group G

in Fig. 3). These compounds can be markers for investigating human uremic symptoms in the rat renal failure model, because the compounds increase commonly both in human and rat renal failure.

On the other hand, several differences were seen between the human and the rat renal failure model. We have identified that 1-methyladenosine, N-acetylglucosamine, γ-butyrobetaine, sebacate, cis-aconitate and homovanillate are good markers for detecting CKD [9]. In ADPKD Cy/+ rats, CE-MS analysis revealed that cis-aconitate was also significantly increased (Figs. 1, 2). 1-Methyladenosine, N-acetylglucosamine, γ-butyrobetaine, sebacate and homovanillate were significantly detected in CKD patients but not in rat renal failure, suggesting that these compounds would be much better markers for detecting only human renal damage (group B in Fig. 3). However, cis-aconitate would be a marker for both rat and human renal damage (group D in Fig. 3) [9].

The concentration of γ-GBA, pipecolate, α-aminoadipate, Gly and carnitine were significantly different in

Springer

Table 3 Fifty-nine anionic compounds detected by CE-MS in +/+ rats and Cy/+ rats

Anionic compound	+/+ rat (μM)	Cy/+ rat (μM)	P value
Decanoate	*9.15 ± 0.19*	*7.20 ± 0.21*	*<0.001*
Hippurate	5.54 ± 1.04	17.51 ± 1.46	**<0.001**
Allantoate	*4.28 ± 0.30*	*10.87 ± 0.99*	*<0.001*
Citrate	97.31 ± 5.38	174.38 ± 12.82	**0.001**
o-Hydroxybenzoate	*1.74 ± 0.09*	*2.98 ± 0.17*	*0.001*
cis-Aconitate	2.48 ± 0.13	3.53 ± 0.17	**0.002**
iso-Citrate	3.40 ± 0.35	6.42 ± 0.58	**0.004**
Phenaceturate	*2.00 ± 0.09*	*3.73 ± 0.41*	*0.006*
3-Phenylpropionate	*7.97 ± 0.38*	*10.19 ± 0.40*	*0.007*
3-Indoxyl sulfate	2.91 ± 0.11	20.25 ± 4.36	**0.007**
trans-Aconitate	0.60 ± 0.07	1.28 ± 0.17	**0.010**
2-Oxoglutarate	35.15 ± 2.98	17.29 ± 4.12	**0.014**
Isethionate	1.83 ± 0.17	3.32 ± 0.40	**0.016**
Octanoate	12.18 ± 0.50	9.87 ± 0.46	**0.016**
2-Oxoisopentanoate	18.68 ± 1.95	12.43 ± 0.65	**0.026**
4-Methyl-2-oxopentanoate	45.19 ± 4.83	30.33 ± 1.54	**0.031**
10-Hydroxydecanoate	*1.61 ± 0.09*	*1.21 ± 0.11*	*0.033*
Pantothenate	2.26 ± 0.11	3.14 ± 0.29	**0.036**
Pimelate	0.48 ± 0.02	0.83 ± 0.13	**0.045**
Pelargonate	13.11 ± 0.39	11.11 ± 0.70	0.058
Cholate	11.96 ± 3.18	20.88 ± 2.06	0.068
Undecanoate	3.75 ± 0.15	3.12 ± 0.22	0.069
Cysteine *S*-sulfate	3.22 ± 0.45	4.28 ± 0.17	0.083
Gluconate	14.43 ± 2.17	22.69 ± 3.35	0.101
Oxamate	2.50 ± 0.15	9.04 ± 3.21	0.106
Cysteine sulfinate	1.02 ± 0.05	1.19 ± 0.01	0.116
Pyruvate	159.60 ± 13.71	129.06 ± 8.19	0.125
N-Acetylmuramate	2.85 ± 0.59	5.27 ± 0.78	0.169
2-Hydroxyisobutyrate, 2-hydroxybutyrate	14.85 ± 0.57	17.22 ± 1.45	0.211
Quinate	13.50 ± 1.06	11.52 ± 0.82	0.222
N-Acetylleucine	0.55 ± 0.04	0.62 ± 0.03	0.231
Mucate	9.35 ± 1.35	6.87 ± 1.08	0.236
3-Phosphoglycerate	1.26 ± 0.47	0.60 ± 0.14	0.285
Glycerophosphate	3.46 ± 0.26	5.59 ± 1.64	0.285
2-Hydroxypentanoate	98.65 ± 3.83	107.02 ± 5.91	0.319
4-Oxohexanoate, 4-acetylbutyrate	12.15 ± 0.83	11.01 ± 0.58	0.345
Heptanoate	9.35 ± 0.64	8.39 ± 0.58	0.350
Sebacate	0.39 ± 0.10	0.28 ± 0.02	0.354
Fructose 6-phosphate, glucose 6-phosphate	4.23 ± 0.68	5.79 ± 1.25	0.355
Succinate	23.51 ± 2.47	42.95 ± 17.93	0.365
Hexanoate	20.63 ± 1.71	18.35 ± 1.43	0.388
Asp	25.65 ± 3.17	29.83 ± 2.78	0.401
N-Acetylglutamate	0.33 ± 0.03	0.38 ± 0.04	0.420
4-Oxopentanoate	5.29 ± 0.60	5.89 ± 0.27	0.442
Lactate	3,652.19 ± 257.54	4,038.92 ± 466.43	0.534
Pentanoate, 3-methylbutanoate	24.55 ± 2.61	22.46 ± 2.13	0.594
5-Oxoproline	33.45 ± 1.65	34.68 ± 1.82	0.667

Table 3 continued

Anionic compound	+/+ rat (μM)	Cy/+ rat (μM)	P value
Glu	155.66 ± 26.57	169.76 ± 16.54	0.698
Sedoheptulose 7-phosphate	1.98 ± 0.59	2.49 ± 0.79	0.701
Benzoate	46.44 ± 1.26	47.08 ± 0.89	0.719
Glutarate	5.89 ± 0.46	6.35 ± 1.05	0.729
Malate	21.64 ± 1.67	23.19 ± 3.52	0.732
Azelate	0.78 ± 0.11	0.83 ± 0.11	0.756
Butanoate	40.65 ± 4.93	38.46 ± 4.04	0.767
Fumarate	5.75 ± 0.71	5.45 ± 0.72	0.801
Glycolate	27.08 ± 1.49	26.65 ± 2.79	0.904
Malonate	2.82 ± 0.22	2.80 ± 0.18	0.959
3-Hydroxybutyrate	144.27 ± 19.17	145.38 ± 14.50	0.968
Terephthalate	0.74 ± 0.05	0.75 ± 0.02	0.973

These compounds are in an ascending order of P value calculated by t test

A value of $P < 0.05$ is accepted as indicating a significant difference in the compound concentration between +/+ rats and Cy/+ rats (19 anions)

Italicized compounds have not been reported before as shown in Table 4

ADPKD Cy/+ rats and the nephrectomized rat model; however, they were not significant in CKD patients [9]. Thus, these compounds would only be markers for rat renal damage (group F in Fig. 3).

We have recently identified uremic solutes in the rat renal failure model [8]. The increases of 4-acetylbutyrate, hexanoate, 2-hydroxypentanoate and argininosuccinate in the rat renal failure model were not detected in CKD patients and Cy/+ rats [9] (group C in Fig. 3).

To date, as far as we know, no report shows the biological mechanism by which uremic solutes differ between humans, renal failure model rats and ADPKD rats, although it may depend on the metabolic pathway or pathophysiological reasons. Further characterization of each uremic solute will also be necessary to reveal specific markers for human ADPKD, because uremic solutes in human CKD are different from the rat renal failure model and those in Cy/+ rats are different from other rat renal failure models.

Different guanidino compounds (GCs) were reported as possible uremic toxins, and the accumulation of guanidino compounds and several uremic toxins generate oxidative stress, causing further renal damage in CKD patients [36–38]. Recently Torremans et al. [7] reported remarkable increases of urea, creatinine, GSA, guanidine, methylguanidine, symmetrical dimethylarginine, ADMA and α-keto-δ-GVA in the blood of PKD/Mhm rats and in human ADPKD. In Cy/+ rats, creatinine, γ-GBA, ADMA and GSA were also significantly increased compared with controls (Table 4). However, we could not find a significant increase of methylguanidine in Cy/+ rats compared to control rats. In addition, we could not technically detecte α-keto-δ-GVA and guanidine.

ADMA, an inhibitor of nitric oxide synthase, is implicated in hypertension, renal damage, cardiac hypertrophy and cardiovascular events in renal failure [39, 40]. In the Cy/+ rat model, ADMA was significantly increased (Fig. 1a; Table 4). Additionally, ADMA tends to correlate with serum UN ($P = 0.08$ using Pearson's correlation coefficient). Because the plasma ADMA level was increased from the early stage in ADPKD patients [41], these data confirm the presence and availability of ADMA as an early marker for ADPKD.

To date, no specific treatment for PKD currently exists; however, several drugs are currently being studied in preclinical and clinical trials. Promising therapeutic agents that have been validated in orthologous animal models have entered clinical trials (statins, angiotensin converting enzyme inhibitors, angiotensin II receptor antagonists, vasopressin V2 receptor antagonists) [42–44]. In the Han:SPRD rat, a 3-hydroxy-3-methylglutaryl-coenzyme A reductase inhibitor, lovastatin, significantly reduced the cystic kidney size, the volume density of cysts and serum UN level, diminishing the severity [45]. Lovastatin therapy also demonstrated structural and functional benefits, including increased renal blood flow and decreased UN, independently of a change in the mean arterial pressure in Han:SPRD rats [42]. Recently, we demonstrated that statins induce the expression of kidney-specific organic anion transporter SLCO4C1 in the kidney and that this upregulation reduced hypertension, cardiomegaly and inflammation in renal failure, together with a reduction of

Table 4 Cationic and anionic compounds whose serum concentrations differ significantly between +/+ rat and Cy/+ rats

Compounds	Reported in renal failure model rat	Reported in CKD patients	Reported in rat by Toyohara T. et al. [8]	Reported in human by Toyohara T. et al. [9]	Reported in ADPKD rat and human by Torremans et al. [7]	Group in Venn diagram	References
Cationic compounds increased in Cy/+ rats (Fig. 1a)							
γ-Guanidinobutyrate (γ-GBA)	O		NS	Low limit	Increased in rat	F	[16]
Creatinine	O	O	O	O	O	G	
Anthranilate		O	Low limit	Low limit		D	[17, 18]
3-Methylhistidine	O	O	O	O		G	[19, 20]
Allantoin	O	O		O		G	[21]
Trimethylamine N-oxide		O	O	O		G	[22]
Pipecolate			O	NS		F	
5-Methyl-2-deoxycytidine			NS	Low limit		A	
Homoarginine: trimethyllysine			NS	NS	Decreased	?	
α-Aminoadipate			O	NS		F	
Hydroxyproline	O	O	NS	O		G	[23, 24]
Glucosamine			NS	NS		A	
Citrulline	O	O	O	O		G	[19, 20]
Ectoine			NS	Low limit		A	
Methionine sulfoxide			Decreased	O		D	
Gly	O		NS	NS		F	[19]
ADMA		O	NS	O		D	[4]
N,N-Dimethylglycine		O	NS	O		D	[25]
o-Acetylcarnitine		O	Low limit	NS		D	[26]
Guanidinosuccinate (GSA)	O	O	O	O	O	G	
Cationic compounds decreased in Cy/+ rats (Fig. 1b)							
2-Deoxycytidine			NS	Low limit		A	
Carnitine			O	NS		F	
Anionic compounds increased in Cy/+ rats (Fig. 3a)							
Hippurate	O	O	NS	O		G	[27, 28]
Allantoate			NS	Low limit		A	
Citrate		O	ND	O		D	[28]
o-Hydroxybenzoate			Low limit	Low limit		A	
cis-Aconitate			NS	O		D	
iso-Citrate			ND	O		D	
Phenaceturate			NS	Low limit		A	
3-Phenylpropionate			NS	Low limit		A	
3-Indoxyl sulfate	O	O	O	O		G	[29]
trans-Aconitate			O	O		G	
Isethionate			NS	O		D	
Pantothenate		O	NS	Low limit		D	[30]
Pimelate			NS	O		D	
Anionic compounds decreased in Cy/+ rats (Fig. 3b)							
Decanoate			NS	NS		A	
2-Oxoglutarate			NS	O		D	
Octanoate			NS	O		D	
2-Oxoisopentanoate			NS	O		D	
4-Methyl-2-oxopentanoate			NS	O		D	
10-Hydroxydecanoate			Low limit	Low limit		A	

The compounds in this table are compared to compounds in published reports. The compounds are classified in the Venn diagram (Fig. 3)

Italicized compounds were identified as the compounds that increase or decrease specifically in Cy/+ rats (group A)

O indicates that the concentration changing of the compounds in renal failure was reported in published reports, our reports or the report by Torremans et al.

Low limit indicates the compound concentration in plasma was lower than the detection limits of CE-MS

NS indicates that the compound concentration was not significantly increased or decreased in renal failure rat or human

ND indicates that the compound concentration was not determined

? indicates that increasing and decreasing of the compound concentration was different between our report and the previous report by Torremans et al. [7]
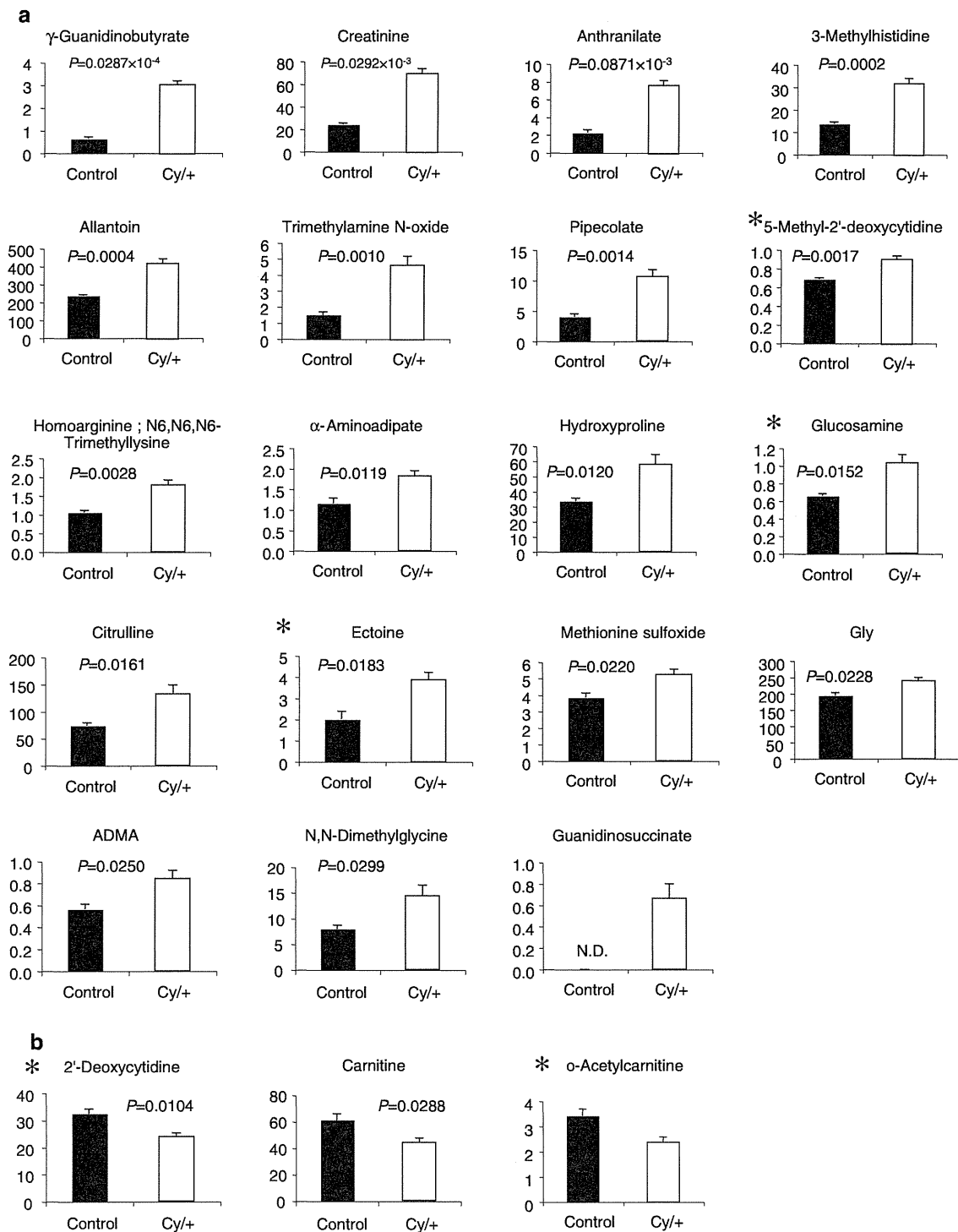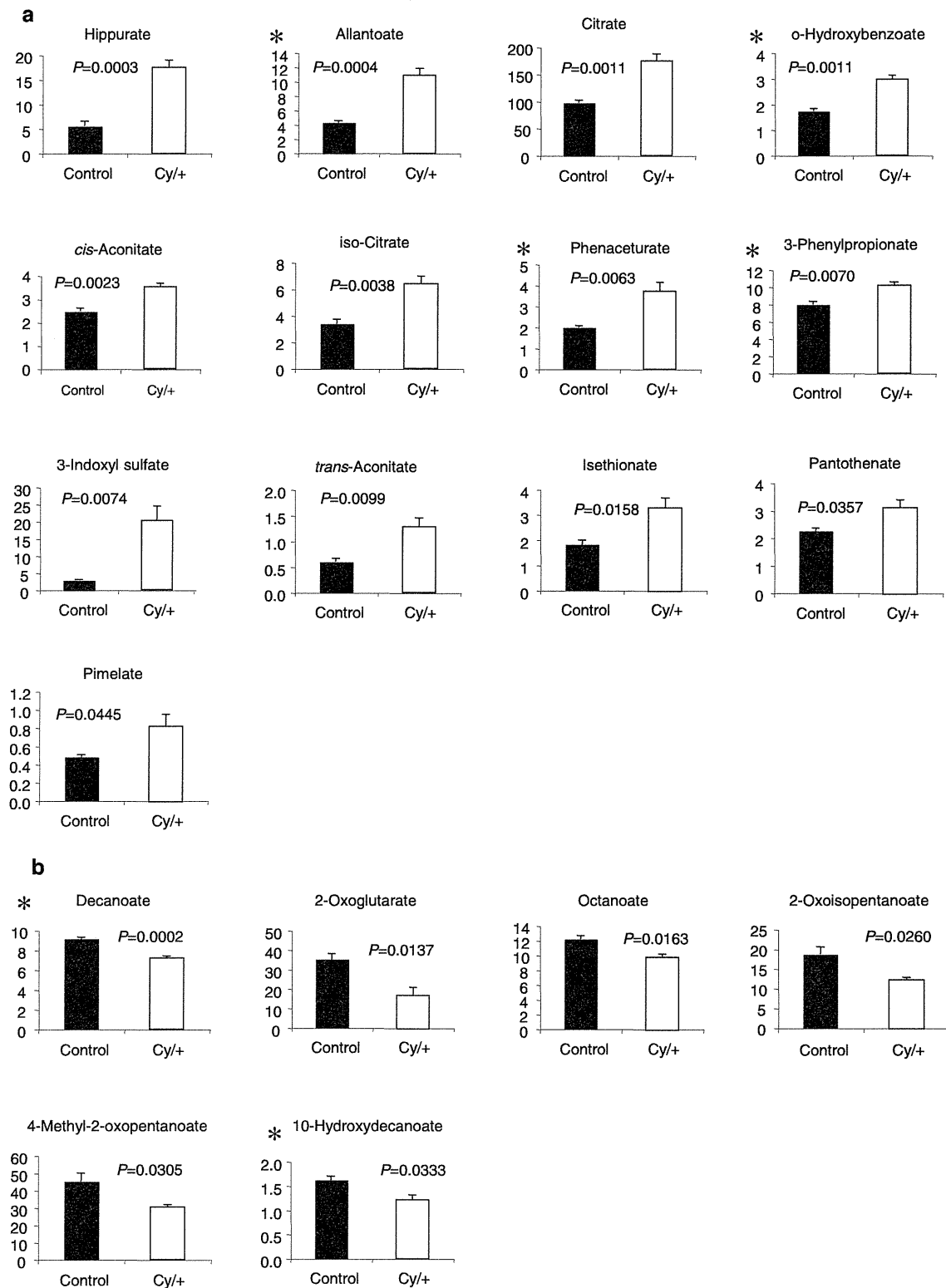
Fig. 1 The cationic compounds whose concentration in Cy/+ rat plasma was significantly increased (**a**) or decreased (**b**) compared to +/+ rats. *Asterisks* indicate newly identified compounds which increase or decrease specifically in Cy/+ rats

the plasma uremic toxins, GSA, ADMA and *trans*-aconitate [8]. Because significantly increased levels of GSA and ADMA were reported in patients with ADPKD [7],

our finding on statins provides a new scientific basis for the pleiotropic effect of statins and a clinical trial in ADPKD patients in the USA (Trial NCT00456365).

Fig. 2 The anionic compounds whose concentration in Cy/+ rat plasma was significantly increased (**a**) or decreased (**b**) compared to +/+ rats. *Asterisks* indicate newly identified compounds which increase or decrease specifically in Cy/+ rats

Statins appear likely to become a new clinical tool for ADPKD patients to decelerate renal damage and delay starting hemodialysis.

In conclusion, we comprehensively identified new uremic solutes in the serum from ADPKD Cy/+ rats and revealed a difference in uremic solutes among human CKD

Rat renal failure model
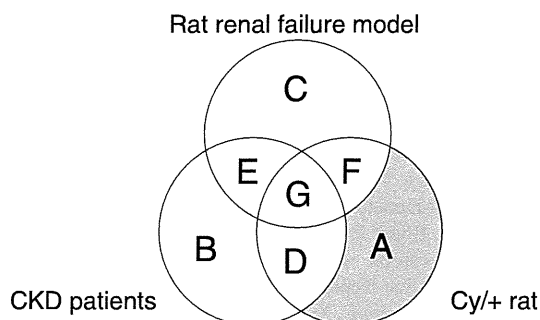
Fig. 3 Venn diagram revealing groups of uremic compounds corresponding to Table 4

patients, the rat renal failure model and Cy/+ rats. We also found new biomarker candidates for detecting renal damage in ADPKD. The results are useful for further studies to elucidate mechanisms accumulating uremic toxins.

References

1. Iglesias CG, Torres VE, Offord KP, Holley KE, Beard CM, Kurland LT. Epidemiology of adult polycystic kidney disease, Olmsted County, Minnesota: 1935–1980. Am J Kidney Dis. 1983;2:630–9.
2. Schrier RW. Optimal care of autosomal dominant polycystic kidney disease patients. Nephrology (Carlton). 2006;11:124–30.
3. Vanholder R, Van Laecke S, Glorieux G. What is new in uremic toxicity? Pediatr Nephrol. 2008;23:1211–21.
4. Marescau B, Nagels G, Possemiers I, De Broe ME, Becaus I, Billiouw JM, Lornoy W, De Deyn PP. Guanidino compounds in serum and urine of nondialyzed patients with chronic renal insufficiency. Metabolism. 1997;46:1024–31.
5. Kielstein JT, Zoccali C. Asymmetric dimethylarginine: a novel marker of risk and a potential target for therapy in chronic kidney disease. Curr Opin Nephrol Hypertens. 2008;17:609–15.
6. Vanholder R, De Smet R, Glorieux G, Argiles A, Baurmeister U, Brunet P, Clark W, Cohen G, De Deyn PP, Deppisch R, Descamps-Latscha B, Henle T, Jorres A, Lemke HD, Massy ZA, Passlick-Deetjen J, Rodriguez M, Stegmayr B, Stenvinkel P, Tetta C, Wanner C, Zidek W. Review on uremic toxins: classification, concentration, and interindividual variability. Kidney Int. 2003;63:1934–43.
7. Torremans A, Marescau B, Kranzlin B, Gretz N, Billiouw JM, Vanholder R, De Smet R, Bouwman K, Brouns R, De Deyn PP. Biochemical validation of a rat model for polycystic kidney disease: comparison of guanidino compound profile with the human condition. Kidney Int. 2006;69:2003–12.
8. Toyohara T, Suzuki T, Morimoto R, Akiyama Y, Souma T, Shiwaku HO, Takeuchi Y, Mishima E, Abe M, Tanemoto M, Masuda S, Kawano H, Maemura K, Nakayama M, Sato H, Mikkaichi T, Yamaguchi H, Fukui S, Fukumoto Y, Shimokawa H, Inui K, Terasaki T, Goto J, Ito S, Hishinuma T, Rubera I, Tauc M, Fujii-Kuriyama Y, Yabuuchi H, Moriyama Y, Soga T, Abe T. Slco4c1 transporter eliminates uremic toxins and attenuates

hypertension and renal inflammation. J Am Soc Nephrol. 2009;20:2546–55.
9. Toyohara T, Akiyama Y, Suzuki T, Takeuchi Y, Mishima E, Tanemoto M, Momose A, Toki N, Sato H, Nakayama M, Hozawa A, Tsuji I, Ito S, Soga T, Abe T. Metabolomic profiling of uremic solutes in CKD patients. Hypertens Res. 2010;33:944–52.
10. Soga T, Ueno Y, Naraoka H, Ohashi Y, Tomita M, Nishioka T. Simultaneous determination of anionic intermediates for *Bacillus subtilis* metabolic pathways by capillary electrophoresis electrospray ionization mass spectrometry. Anal Chem. 2002;74:2233–9.
11. Mikkaichi T, Suzuki T, Onogawa T, Tanemoto M, Mizutamari H, Okada M, Chaki T, Masuda S, Tokui T, Eto N, Abe M, Satoh F, Unno M, Hishinuma T, Inui K, Ito S, Goto J, Abe T. Isolation and characterization of a digoxin transporter and its rat homologue expressed in the kidney. Proc Natl Acad Sci USA. 2004; 101:3569–74.
12. Schafer K, Gretz N, Bader M, Oberbaumer I, Eckardt KU, Kriz W, Bachmann S. Characterization of the Han:SPRD rat model for hereditary polycystic kidney disease. Kidney Int. 1994; 46:134–52.
13. Nagao S, Ushijima T, Kasahara M, Yamaguchi T, Kusaka M, Matsuda J, Nagao M, Takahashi H. Closely linked polymorphic markers for determining the autosomal dominant allele (cy) in rat polycystic kidney disease. Biochem Genet. 1999;37:227–35.
14. Soga T, Ohashi Y, Ueno Y, Naraoka H, Tomita M, Nishioka T. Quantitative metabolome analysis using capillary electrophoresis mass spectrometry. J Proteome Res. 2003;2:488–94.
15. Soga T, Heiger DN. Amino acid analysis by capillary electrophoresis electrospray ionization mass spectrometry. Anal Chem. 2000;72:1236–41.
16. Soga T, Igarashi K, Ito C, Mizobuchi K, Zimmermann HP, Tomita M. Metabolomic profiling of anionic metabolites by capillary electrophoresis mass spectrometry. Anal Chem. 2009; 81(15):6165–74.
17. Levillain O, Marescau B, de Deyn PP. Guanidino compound metabolism in rats subjected to 20% to 90% nephrectomy. Kidney Int. 1995;47:464–72.
18. Pawlak D, Pawlak K, Malyszko J, Mysliwiec M, Buczko W. Accumulation of toxic products degradation of kynurenine in hemodialyzed patients. Int Urol Nephrol. 2001;33:399–404.
19. Pawlak D, Tankiewicz A, Buczko W. Kynurenine and its metabolites in the rat with experimental renal insufficiency. J Physiol Pharmacol. 2001;52:755–66.
20. Swendseid ME, Wang M, Vyhmeister I, Chan W, Siassi F, Tam CF, Kopple JD. Amino acid metabolism in the chronically uremic rat. Clin Nephrol. 1975;3:240–6.
21. Ceballos I, Chauveau P, Guerin V, Bardet J, Parvy P, Kamoun P, Jungers P. Early alterations of plasma free amino acids in chronic renal failure. Clin Chim Acta. 1990;188:101–8.
22. Amathieu R, Racine S, Triba M, Poloujadoff MP, Borron SW, Bouchemal N, Lapostolle F, Merouani M, Le Moyec L, Adnet F. Use of nuclear magnetic resonance spectroscopy to assess renal dysfunction after hypertonic-hyperoncotic resuscitation in rats. J Trauma. 2007;63:379–87.
23. Bain MA, Faull R, Fornasini G, Milne RW, Evans AM. Accumulation of trimethylamine and trimethylamine-*N*-oxide in end-stage renal disease patients undergoing haemodialysis. Nephrol Dial Transplant. 2006;21:1300–4.
24. Shimizu T, Fukagawa M, Kuroda T, Hata S, Iwasaki Y, Nemoto M, Shirai K, Yamauchi S, Margolin SB, Shimizu F, Kurokawa K. Pirfenidone prevents collagen accumulation in the remnant kidney in rats with partial nephrectomy. Kidney Int Suppl. 1997; 63:S239–43.
25. Hart W, Duursma SA, Visser WJ, Njio LK. The hydroxyproline content of plasma of patients with impaired renal function. Clin Nephrol. 1975;4:104–8.

26. McGregor DO, Dellow WJ, Lever M, George PM, Robson RA, Chambers ST. Dimethylglycine accumulates in uremia and predicts elevated plasma homocysteine concentrations. Kidney Int. 2001;59:2267–72.

27. Evans AM, Faull RJ, Nation RL, Prasad S, Elias T, Reuter SE, Fornasini G. Impact of hemodialysis on endogenous plasma and muscle carnitine levels in patients with end-stage renal disease. Kidney Int. 2004;66:1527–34.

28. Deguchi T, Takemoto M, Uehara N, Lindup WE, Suenaga A, Otagiri M. Renal clearance of endogenous hippurate correlates with expression levels of renal organic anion transporters in uremic rats. J Pharmacol Exp Ther. 2005;314:932–8.

29. Farrell PC, Gotch FA, Peters JH, Berridge BJ Jr, Lam M. Binding of hippurate in normal plasma and in uremic plasma pre- and postdialysis. Nephron. 1978;20:40–6.

30. Niwa T, Ise M. Indoxyl sulfate, a circulating uremic toxin, stimulates the progression of glomerular sclerosis. J Lab Clin Med. 1994;124:96–104.

31. DeBari VA, Frank O, Baker H, Needle MA. Water soluble vitamins in granulocytes, erythrocytes, and plasma obtained from chronic hemodialysis patients. Am J Clin Nutr. 1984;39:410–5.

32. Lee SH, Kim I, Chung BC. Increased urinary level of oxidized nucleosides in patients with mild-to-moderate Alzheimer's disease. Clin Biochem. 2007;40:936–8.

33. Becker BF. Towards the physiological function of uric acid. Free Radic Biol Med. 1993;14:615–31.

34. Hwang SY, Shin JH, Hwang JS, Kim SY, Shin JA, Oh ES, Oh S, Kim JB, Lee JK, Han IO. Glucosamine exerts a neuroprotective effect via suppression of inflammation in rat brain ischemia/reperfusion injury. Glia. 2010;58:1881–92.

35. Roberts MF. Organic compatible solutes of halotolerant and halophilic microorganisms. Saline Syst. 2005;1:5.

36. Cachofeiro V, Goicochea M, de Vinuesa SG, Oubina P, Lahera V, Luno J. Oxidative stress and inflammation, a link between chronic kidney disease and cardiovascular disease. Kidney Int Suppl. 2008;74:S4–9.

37. D'Hooge R, Raes A, Lebrun P, Diltoer M, Van Bogaert PP, Manil J, Colin F, De Deyn PP. N-methyl-D-aspartate receptor activation by guanidinosuccinate but not by methylguanidine: behavioural and electrophysiological evidence. Neuropharmacology. 1996;35:433–40.

38. Vanholder R, De Smet R. Pathophysiologic effects of uremic retention solutes. J Am Soc Nephrol. 1999;10:1815–23.

39. Zoccali C, Benedetto FA, Maas R, Mallamaci F, Tripepi G, Malatino LS, Boger R. Asymmetric dimethylarginine, C-reactive protein, and carotid intima-media thickness in end-stage renal disease. J Am Soc Nephrol. 2002;13:490–6.

40. Fliser D, Kronenberg F, Kielstein JT, Morath C, Bode-Boger SM, Haller H, Ritz E. Asymmetric dimethylarginine and progression of chronic kidney disease: the mild to moderate kidney disease study. J Am Soc Nephrol. 2005;16:2456–61.

41. Wang D, Strandgaard S, Borresen ML, Luo Z, Connors SG, Yan Q, Wilcox CS. Asymmetric dimethylarginine and lipid peroxidation products in early autosomal dominant polycystic kidney disease. Am J Kidney Dis. 2008;51:184–91.

42. Zafar I, Tao Y, Falk S, McFann K, Schrier RW, Edelstein CL. Effect of statin and angiotensin-converting enzyme inhibition on structural and hemodynamic alterations in autosomal dominant polycystic kidney disease model. Am J Physiol Renal Physiol. 2007;293:F854–9.

43. Schrier RW. Renal volume, renin-angiotensin-aldosterone system, hypertension, and left ventricular hypertrophy in patients with autosomal dominant polycystic kidney disease. J Am Soc Nephrol. 2009;20:1888–93.

44. Patel V, Chowdhury R, Igarashi P. Advances in the pathogenesis and treatment of polycystic kidney disease. Curr Opin Nephrol Hypertens. 2009;18:99–106.

45. Gile RD, Cowley BD Jr, Gattone VH 2nd, O'Donnell MP, Swan SK, Grantham JJ. Effect of lovastatin on the development of polycystic kidney disease in the Han:SPRD rat. Am J Kidney Dis. 1995;26:501–7.

Cyclin D2 in the basal process of neural progenitors is linked to non-equivalent cell fates

Yuji Tsunekawa[1], Joanne M Britto[2],
Masanori Takahashi[1], Franck Polleux[3],
Seong-Seng Tan[2] and Noriko Osumi[1,*]

[1]Division of Developmental Neuroscience, United Core Centers for
Advanced Research and Translational Medicine, Tohoku University
Graduate School of Medicine, Sendai, Japan, [2]Brain Development and
Regeneration Laboratory, Florey Neuroscience Institutes, University of
Melbourne, Melbourne, Victoria, Australia and [3]Department of Cell
Biology, Dorris Neuroscience Center, The Scripps Research Institute,
La Jolla, CA, USA

Asymmetric cell division plays an indispensable role during corticogenesis for producing new neurons while maintaining a self-renewing pool of apical progenitors. The cellular and molecular determinants favouring asymmetric division are not completely understood. Here, we identify a novel mechanism for generating cellular asymmetry through the active transportation and local translation of *Cyclin D2* mRNA in the basal process. This process is regulated by a unique *cis*-regulatory sequence found in the 3′ untranslated region (3′UTR) of the mRNA. Unequal inheritance of Cyclin D2 protein to the basally positioned daughter cell with the basal process confers renewal of the apical progenitor after asymmetric division. Conversely, depletion of Cyclin D2 in the apically positioned daughter cell results in terminal neuronal differentiation. We demonstrate that Cyclin D2 is also expressed in the developing human cortex within similar domains, thus indicating that its role as a fate determinant is ancient and conserved.

Introduction

During cortical development in mammals, the expansion of the cortical wall relies on large numbers of neurons to be generated by proliferating neuroepithelial cells (Smart, 1973). At early stages of corticogenesis (embryonic day 10.5 (E10.5)), these neuroepithelial cells divide symmetrically to yield more progenitors, resulting in a thickened pseudostratified sheet where the mitotic cells are concentrated mainly

*Corresponding author. Division of Developmental Neuroscience,
United Core Centers for Advanced Research and Translational Medicine,
Tohoku University School of Medicine, 2-1 Seiryo-machi, Aoba-ku,
Sendai 980-8575, Japan. Tel.: +81 22 717 8201; Fax: +81 22 717 8205;
E-mail: osumi@med.tohoku.ac.jp

on the apical side of the epithelium (Rakic, 1988). The dividing cells attached to the apical membrane are called apical progenitors (APs), and during the proliferative stage they undergo mostly symmetric cell divisions, producing daughter cells with equal fates (as neurons or more progenitors) (Huttner and Kosodo, 2005). Later in corticogenesis (E12.5–15.5), neuroepithelial cells become radial glia and start to divide asymmetrically, producing an AP with self-renewing capacity together with a terminally differentiated neuron or intermediate progenitor (IP) (Gotz and Huttner, 2005). Newly produced neurons migrate out of the ventricular zone (VZ) to form the cortical plate (CP), while intermediate progenitors divide symmetrically in the subventricular zone (SVZ) and generate more IPs or neurons (Haubensak et al, 2004; Miyata et al, 2004; Noctor et al, 2004). APs undergoing symmetric and asymmetric divisions often overlap and coexist in the germinal zones (Huttner and Kosodo, 2005), but what is unclear is the motivation driving symmetric versus asymmetric divisions (Gotz and Huttner, 2005).

Asymmetric cell division of neural progenitor cells is critical for establishing the architectures of the mammalian cerebral cortex by regulating the balance between proliferative and neurogenic populations. This is achieved by producing daughter cells that are self-renewing together with daughter cells that become postmitotic neurons and thereby increasing the number of neurons while maintaining the number of APs (Gotz and Huttner, 2005; Kriegstein et al, 2006). In addition, asymmetric cell division is capable of generating a third class of offspring known as the intermediate progenitor whose cell body lies in the SVZ and retracts its apical attachment prior to mitosis (Miyata et al, 2004; Attardo et al, 2008). These observations invite the question—what cellular factors influence mitotic descendants to become a self-renewing AP or a differentiated neuron?

A key issue in this debate concerns the roles played by structural elements such as the apical membrane or basal process, and their cytoplasmic constituents, in conferring AP fate. The cleavage plane *per se* is not an indicator of symmetric or asymmetric division (Kosodo et al, 2004), but experimental randomization of the cleavage plane (by changing mitotic spindle orientation) decreases the number of APs (Konno et al, 2008). Leaving cleavage plane aside, it has been suggested that asymmetric inheritance of fate-determining constituents present in the apical process is sufficient to ensure asymmetric division (Kosodo et al, 2004; Attardo et al, 2008; Bultje et al, 2009), but this notion has been undermined by a recent study showing that even complete inheritance of the apical process is no guarantor of AP fates (Konno et al, 2008). In this context, the status of the basal process has been underexplored, although it has been hypothesized that inheritance of both apical and basal processes is required for self-renewing capability (Konno et al, 2008). Certainly, basal process splitting has been observed to accompany both symmetric and asymmetric neuroepithelial

divisions (Kosodo et al, 2008; Kosodo and Huttner, 2009), although there is controversy whether asymmetric inheritance of the basal process is predictive of neuronal differentiation (Miyata et al, 2001) or progenitor renewal (Ochiai et al, 2009; Alexandre et al, 2010).

In the current study, we set out to explore the role of the basal process, in particular the contribution by the polarized distribution of Cyclin D2, in the determination of apical progenitor fate. Previous studies have established that Cyclin D2 protein localized in the basal process of neural progenitors (Glickstein et al, 2007), and as a member of the Cyclin family, may be involved in the regulation of the cell cycle (Dehay and Kennedy, 2007; Salomoni and Calegari, 2010). Other studies have established that another family member, Cyclin D1, is implicated in regulating the balance between the number of cortical cells undergoing proliferation or becoming IPs (Lange et al, 2009). Here, we demonstrate using mouse cortical tissue the polarized distribution of Cyclin D2 mRNA and protein in neural progenitors. We identify a novel 50 base pair (bp) cis-acting transport element for the basal localization of Cyclin D2 mRNA within its 3' untranslated region (3'UTR) and showed that Cyclin D2 mRNA is locally translated into protein at the basal endfoot. We provide several lines of evidence to suggest that post-transcriptional regulatory systems are required for asymmetric segregation of Cyclin D2 protein to one of the two daughter cells. In addition, gain- and loss-of-function experiments that perturb asymmetrical distribution of Cyclin D2 protein in apical progenitor cells severely distort asymmetry of the cell fate. Finally, we show that protein localization of Cyclin D2 is highly conserved in the human fetal cortex. Taken together, we propose a model for Cyclin D2 as a fate determinant by the asymmetrical distribution of Cyclin D2 to the basal process and subsequent inheritance to the mitotic offspring with self-renewing capacity.

Results

Localization patterns of Cyclin D2 mRNA and protein during early corticogenesis

Localization of Cyclin D2 protein in the developing neocortex has been previously reported (Ross et al, 1996; Glickstein et al, 2007), while detailed subcellular distributions with regard to developmental periods and cell-cycle phases have not been elucidated. We first examined changes in the expression patterns of Cyclin D2 mRNA and protein in mouse forebrain during the proliferation (E10.5) and neurogenic stages (E14.5). Antibody specificity was confirmed by western blotting and immunostaining on Cyclin D2 knockout mouse neocortex with wild-type littermates (Supplementary Figure S1).

From E10.5 to E14.5, Cyclin D2 mRNA was detected in the cortical wall, mostly near the basal lamina as reported by others, and weakly in the VZ (Figure 1A–C). In comparison, mRNA of another members of the Cyclin family, Cyclin D1 and Cyclin D3, was present in the VZ but not at the basal edge of the cortical primordium (Supplementary Figure S2). At higher magnification, expression of Cyclin D2 mRNA and protein in the cortical wall showed unique and differential patterns. Cyclin D2 mRNA was preferentially localized in subcellular structures adjacent to the basal lamina at all three stages examined (Figure 1D, F and H). On the other hand, the protein was evenly distributed in cellular nuclei of

the epithelial sheet at E10.5 (Figure 1E), but at older stages (E12.5 and 14.5) the protein showed a dual distribution pattern directed at basal processes and VZ cells with little staining in between (Figure 1G and I). At these stages, Cyclin D2 protein in the VZ and SVZ was found in the nucleus (arrow in inset of Figure 1G), although not all cells were immunopositive (double arrow in inset of Figure 1G). Even though Cyclin D2 protein was expressed in nuclear and non-nuclear compartments, Cyclin D2 mRNA itself was consistently found in cytoplasmic structures on the basal but not apical aspects of the neuroepithelium.

To confirm Cyclin D2 mRNA and protein were expressed in neural progenitor cells, fluoro in-situ hybridization with immunostaining and double immunostaining of Cyclin D2 mRNA and protein with βIII-tubulin (which marks neurons) was performed in the E12.5 cortex. The results show that Cyclin D2 mRNA and protein localization in basal structures was essentially non-neuronal (Figure 1J and K, arrowheads). Instead, double immunocytochemistry with laminin indicates that Cyclin D2 staining was not coextensive with the basement membrane (Figure 1L), but restricted in the basal endfoot of neuroepithelial cells revealed by EGFP-lentiviral reporter (Figure 1M and N). Thus, polarized Cyclin D2 expression in the basal processes of neural progenitors appears during the onset of neurogenesis, and is maintained thereafter.

A cis-acting transport element of Cyclin D2 mRNA resides in its 3' UTR

To elucidate the mechanism behind the polarized distribution of Cyclin D2 mRNA in cortical progenitor cells, whole-embryo cultures and electroporation experiments were conducted (Supplementary Figure S3A; Osumi and Inoue, 2001). Since localization of mRNA is usually achieved by the binding of a cis-acting transport element with a trans-acting localization factor (Palacios and St Johnston, 2001), we tested whether a cis-acting transport element is present in the 3'UTR of Cyclin D2 (AK147345). A reporter construct, pCE/CD2/3', was generated by inserting the entire 3'UTR region of Cyclin D2 mRNA (1106–6274) into an open reading frame (ORF) downstream of EGFP in pCAX. This construct was co-electroporated with pCAGGS-mRFP into the diencephalon of E12.5 embryos, which were subsequently cultured for 12 h (Supplementary Figure S3A). Localization of transcribed mRNAs was detected by in-situ hybridization using EGFP and mRFP riboprobes on adjacent sections from electroporated embryos. The results demonstrate that EGFP mRNA fused with a Cyclin D2 3'UTR sequence was distributed both in the VZ and in the basal endfoot of neural progenitor cells (Figure 2A), while mRFP mRNA without a Cyclin D2 3'UTR sequence was present only in the VZ (Figure 2B). This suggests that a cis-acting transport element of Cyclin D2 mRNA is present in its 3'UTR region and is capable of transporting reporter mRNA into the basal endfeet. The speed of this transport event (distance of 400 μm in the basal process within 12 h) suggests that passive diffusion or lack of mRNA degradation is unlikely to account for the observed polarized distribution of Cyclin D2 mRNA. Further characterization of this sequence by the use of truncated fragments of the Cyclin D2 3'UTR yielded a minimal 50 bp element (pCE/CD2/3'/3965-4015) that was sufficient for basal localization of Cyclin D2 mRNA, both in the diencephalon and in the cortex (Figure 2C and D;
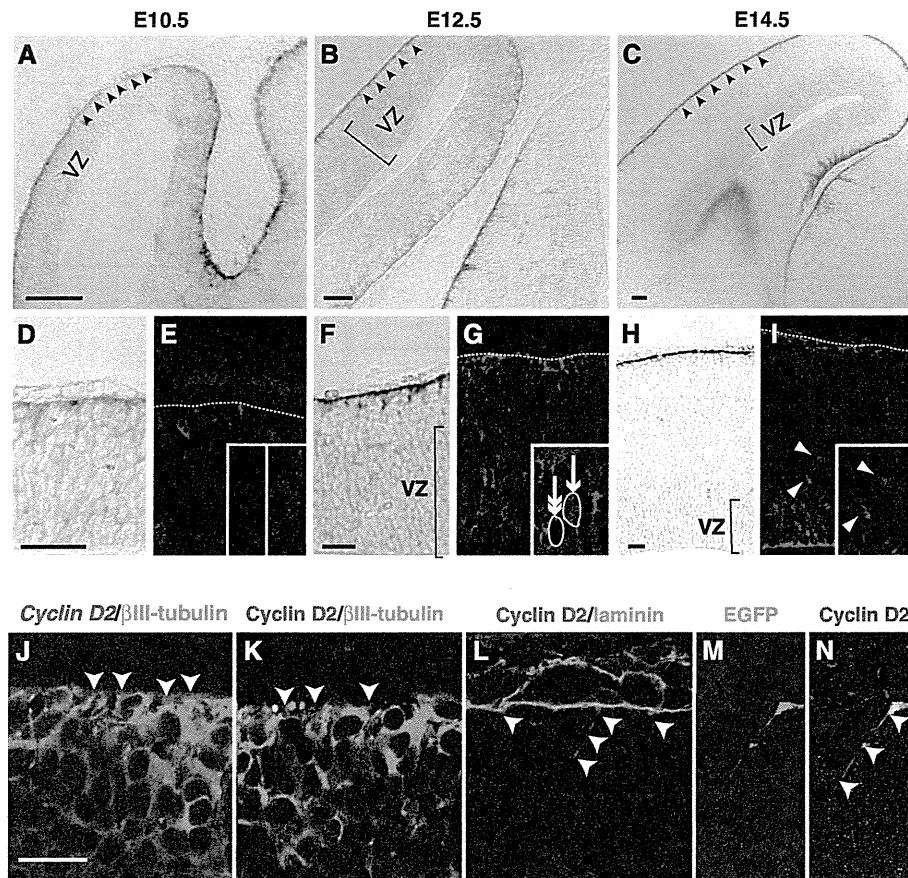
Figure 1 Expression patterns of *Cyclin D2* mRNA and protein during cortical development. (A–I) Localization of *Cyclin D2* mRNA and protein in sections from mouse embryonic neocortex demonstrated by *in-situ* hybridization and immunostaining. At E10.5, *Cyclin D2* mRNA is mainly observed at the basal edge of the neuroepithelium (arrowheads in **A**, higher magnification in **D**), whereas Cyclin D2 protein appears to be uniformly distributed in the nuclei across the epithelial sheet (inset in **E**). At E12.5 and E14.5, *Cyclin D2* mRNA is preferentially expressed on the basal side of radial glia including the basement membrane (**F, H**). In contrast, Cyclin D2 protein is strongly expressed in structures next to the basal lamina (**G, I**), as well as in the VZ where cells showing strong nuclear staining (inset in **G**, arrow) are situated next to other cells devoid of Cyclin D2 protein (inset in **G**, double arrows). A similar distribution pattern is observed at E14.5 with the additional observation that SVZ cells contain Cyclin D2 protein (**I**, arrowheads). (J–L) Double immunostaining in E12.5 cortex shows that *Cyclin D2* mRNA (**J**) and protein (**K**) is found in basal endfeet of non-neuronal processes identified by the lack of βIII-tubulin (**J** and **K**, arrowheads). Cyclin D2 protein is detected in the apical side of the basal lamina revealed by laminin immunoreactivity (arrowheads in **L**), and also in the basal process and endfoot of radial glia revealed by EGFP-lentiviral infection (**M** and **N**, arrowheads). Dotted lines denote the location of the basal lamina, VZ, ventricular zone. Scale bars: 100 μm in (A–C), 50 μm in (D–I), and 20 μm in (J–N).

Supplementary Figure S3B and C). This finding indicates that a 3′UTR transport element regulates the active transport of *Cyclin D2* mRNA to the basal endfeet.

Transported *Cyclin D2* mRNA is translated locally in the basal endfoot

To examine whether the *Cyclin D2* mRNA in the basal endfeet is translated *in situ*, an expression vector, *pCEN/CD2/3′/1496-5457*, containing EGFP with a nuclear localization signal (NLS-EGFP) was electroporated together with *pCAGGS-mRFP* into E13.5 forebrain *in utero* (Takahashi *et al*, 2002; Figure 3A). A construct containing *Cyclin D2* 3′UTR nucleotides 1496–5457 placed downstream of NLS-EGFP in a reverse direction (*pCEN/CD2/3′/5457-1496*) was used as a control for these experiments (Figure 3A). Following fixation 24 h later, *NLS-EGFP* mRNA linked to *Cyclin D2* 3′UTR (1496–5457) was observed at the basal endfeet (Figure 3B and B′), while the control mRNA was located only at the VZ with no

polarized distribution to the basal endfeet (Figure 3E and E′). At the protein level, EGFP translated from *pCEN/CD2/3′/1496-5457* was present at the basal endfeet and ventricular nuclei (Figure 3C and C′), whereas EGFP translated from *pCEN/CD2/3′/5457-1496* was present only in nuclei but undetected in the basal endfeet (Figure 3F and F′). From this line of investigation, we predicted that the translated EGFP would be immediately transported into the nucleus via its NLS. However, this is not the case and localization was also noted in the basal endfoot. It has been reported that translation systems, such as ribosomes, are localized at the basal endfoot of the neural progenitor cells (Astrom and Webster, 1991); and therefore, we can conclude that the EGFP observed at the basal endfoot is locally translated and driven by the presence of the *Cyclin D2* 3′UTR. Co-expressed mRFP was seen in the basal processes and basal endfeet, confirming visible observation of the reporter in the endfeet (Figure 3D, D′, G, and G′).
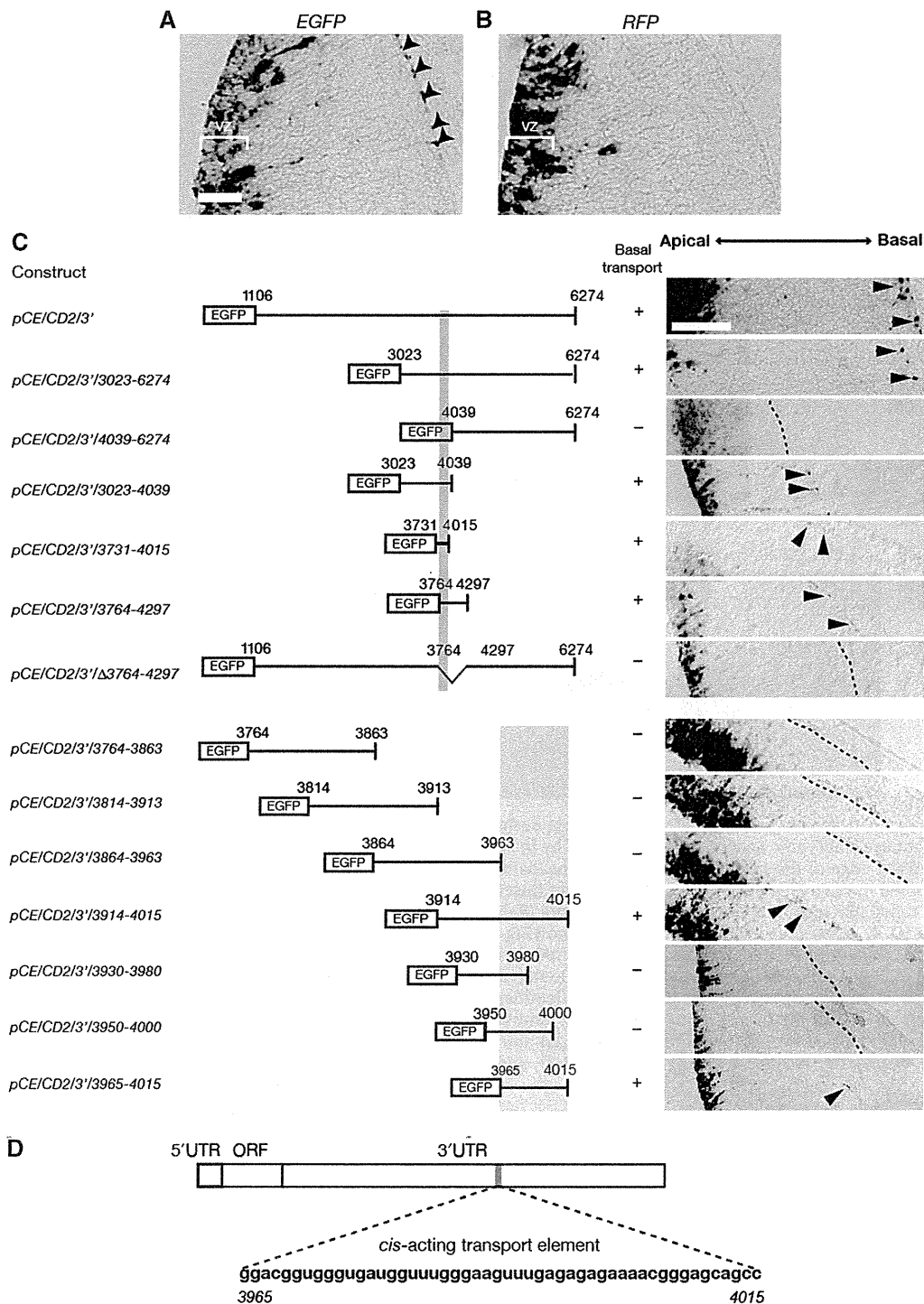
Figure 2 *Cyclin D2* mRNA contains a *cis*-acting transport element in the 3′ untranslated region. *In-situ* hybridization for *EGFP* (**A**) and *RFP* mRNA (**B**), coded by *pCE/CD2/3′* and *pCAGGS-mRFP*, respectively, following electroporation at E12.5. *EGFP* mRNA is found in the VZ as well as in the basal process and the basal endfoot of the radial glia (arrowheads in **A**). In contrast, *RFP* mRNA without *Cyclin D2* 3′UTR is only found in the VZ without expression in the basal process (**B**). (**C**) Identification of a 50 nucleotide *cis*-acting mRNA transport element in the *Cyclin D2* 3′ UTR. Left panel, regions of the *Cyclin D2* 3′ UTR fused with *EGFP* ORF, right panel shows localization of *EGFP-CyclinD2* 3′UTR chimeric mRNA in the mouse diencephalon. (**D**) Diagrammatic representation of *Cyclin D2* mRNA and *cis*-acting transport element (3965–4015). VZ, ventricular zone. Scale bar: 100 μm.

Cyclin D2 protein is asymmetrically inherited by one of the two daughter cells

During asymmetric progenitor division, the basal process is inherited by one of its two daughter cells (Miyata *et al*, 2001; Noctor *et al*, 2001). This poses the question of whether the Cyclin D2 protein is also asymmetrically inherited, and if so,

to which daughter cell does the Cyclin D2-containing basal process belong to? To address this, Cyclin D2 protein was analysed in the basal process and cell body of mitotic off-spring revealed by EGFP-lentiviral infection of E11.5 embryos examined 24 h later. The viral titre used was sufficiently low to produce an infected clone (with 1–3 cells) per cortical